Fe$_x$Ni$_{(1-x)}$ coatings electrodeposited from choline chloride-urea mixture: Magnetic and electrocatalytic properties for water electrolysis

Francisco G.S. Oliveira [a,b,*], Luis P.M. Santos [a,b], Rodolfo B. da Silva [c], Marcio A. Correa [c], Felipe Bohn [c], Adriana N. Correia [d], Luciana Vieira [e], Igor F. Vasconcelos [a,b], Pedro de Lima-Neto [a,d]

[a] Pós-Graduação em Engenharia e Ciências de Materiais, Centro de Tecnologia, Universidade Federal do Ceará, Campus do Pici, Bloco 729, 60440-900, Fortaleza, CE, Brazil
[b] Departamento de Engenharia Metalúrgica e de Materiais, Centro de Tecnologia, Universidade Federal do Ceará, Campus do Pici, Bloco 729, 60440-900, Fortaleza, CE, Brazil
[c] Departamento de Física, Universidade Federal do Rio Grande do Norte, 59078-970, Natal, RN, Brazil
[d] Departamento de Química Analítica e Físico-Química, Centro de Ciências, Universidade Federal do Ceará, Campus do Pici, Bloco 940, 60440-900, Fortaleza, CE, Brazil
[e] Fraunhofer-Institut für Grenzflächen- und Bioverfahrenstechnik IGB, Bio-, Elektro- und Chemokatalyse - BioCat, Schulgasse 11a, 94315, Straubing, Germany

HIGHLIGHTS

- Fe, Ni, and Fe$_x$Ni$_{(1-x)}$ coatings were successfully electrodeposited on Cu from eutectic mixture choline chloride-urea.
- Fe-Ni-based electrocatalysts were prepared by a simplified method and environmentally friendly.
- Fe$_x$Ni$_{(1-x)}$ electrocatalysts showed good electrocatalytic activity and stability for water electrolysis.

GRAPHICAL ABSTRACT
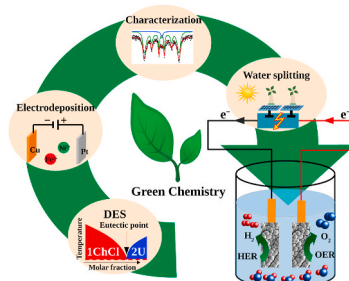
ARTICLE INFO

ABSTRACT

Fe, Ni, and Fe$_x$Ni$_{(1-x)}$ coatings were successfully electrodeposited on Cu substrates from a choline chloride-urea eutectic solution without the addition of complexing agents. In addition, its magnetic properties and electrocatalytic performance for both hydrogen evolution reaction (HER) and oxygen evolution reaction (OER) were fully investigated. X-ray diffraction and Mössbauer spectroscopy analyses characterized the formation of Fe-Ni alloys in the following coatings: Fe$_{89}$Ni$_{11}$, Fe$_{69}$Ni$_{31}$, Fe$_{47}$Ni$_{53}$, and Fe$_{28}$Ni$_{72}$. The magnetic measurements showed that all electrodeposits presented low coercivity, characterizing the coatings as soft magnetic materials. The Fe coating presented the best electrocatalytic performance for HER and OER in 0.5 mol L^{-1} NaOH and at 298.15 K. However, the Fe coating detached from the substrate when it was submitted to a long-term test. Among the Fe$_x$Ni$_{(1-x)}$ coatings, the Fe$_{89}$Ni$_{11}$ coating displayed the best performance for HER since it exhibited the lowest overpotential of 152 mV at an applied current density of 10 mA cm^{-2}. For OER, the Fe$_{69}$Ni$_{31}$ and Fe$_{47}$Ni$_{53}$ were the best electrocatalysts, which presented the highest exchange current densities about of 7×10^{-4} mA cm^{-2} and

* Corresponding author. Pós-Graduação em Engenharia e Ciências de Materiais, Centro de Tecnologia, Universidade Federal do Ceará, Campus do Pici, Bloco 729, 60440-900, Fortaleza, CE, Brazil.
E-mail address: gilvane@alu.ufc.br (F.G.S. Oliveira).

overpotential values around 374 and 377 mV to provide 10 mA cm^{-2}. Furthermore, the Ni and Fe$_x$Ni$_{(1-x)}$ coatings presented good stability in 120 h long term tests at 50 mA cm^{-2}. Finally, the experimental results showed that the manufacture of electrocatalysts based on Fe, Ni and Fe-Ni coatings via electrodeposition conducted in the presence of choline chloride-urea is very promising and environmentally friendly process.

1. Introduction

In 2019, the Intergovernmental Panel on Climate Change (IPCC) published a special report about the global warming of 1.5 °C, revealing that climate change is already affecting people, ecosystems, and livelihoods worldwide [1]. The IPCC also reported that the global energy sector is responsible for most greenhouse gas emissions each year, mainly because the world's energy matrix is strictly based on fossil fuels [2]. Therefore, the scientific community is dedicated to find new energy resources that are clean and renewable to reduce our dependence on the fossil fuels. In this scenario, water electrolysis has emerged as one of the most promising approaches to achieve efficient energy conversion and storage, since it produces hydrogen and oxygen gases at the cathode [3, 4] and at the anode [3–8] of an electrochemical cell, respectively. Furthermore, it can be coupled with several important electrochemical processes such as rechargeable metal-air batteries and regenerative fuel cells [9].

The water electrolysis process is severely limited by the oxygen evolution reaction (OER), which is kinetically sluggish and requires a large overpotential to overcome the activation energy barrier [10]. Therefore, OER is responsible for the most energy consumption during water splitting [11]. In this context, high efficiency electrocatalyst materials must be sought to reduce the energetic cost of the water electrolysis process. Currently, the best performances are found in materials based on precious metals, such as Pt, Pd, and Au [3,4,12], which are rare in the Earth's crust and have high financial costs. Over the last decades, transition-metals-based oxides have opened a new avenue for research of electrocatalysts used in the electrochemical water splitting process [14–19]. For instance, RuO$_2$ and IrO$_2$ have demonstrated high electrocatalytic activities for OER in both acidic and alkaline solutions [5,6, 19]. However, these oxides are scarce in the Earth's crust and have a high cost, which largely restricts their large-scale applications. In contrast, transition metal oxides are more accessible and economically viable. Among them, the oxides of Ni [14,20], Fe [14,21], Co [13,17], and Mn [15] have shown a high potential for water splitting applications, mainly due to their chemical stabilities. Yuan et al. [20] reported the successful application of ferrite NiFe$_2$O$_4$ tubular microstructures for HER and OER, which presented high electrocatalytic activity in a 1.0 mol L^{-1} KOH solution. Moreover, the electrocatalyst performance of this oxide was sensitive to the structural properties of the oxide, as well as its morphology.

In addition, binary alloys based on transition-metals have emerged as promising materials for water electrolysis due to their high stability and excellent electrochemical activity in alkaline solutions [22]. In this context, Fe-Ni binary alloys stand out for presenting excellent electrocatalytic performance associated with chemical stability, either HER and/or OER [23–27]. Luo et al. [26] reported that Fe-Ni electrodeposited alloy exhibited morphology of nanosheets with high catalytic activity and stability for HER, with an overpotential of 139 mV at 10 mA cm^{-2} in 1.0 mol L^{-1} KOH. Ullal et al. [24] in turn electrodeposited Fe-Ni coatings on Cu substrates and tested them for HER and OER, as well as their corrosion resistance in the 6.0 mol L^{-1} KOH, showing excellent efficiency in both situations. Therefore, Fe-Ni alloy has exhibited high stability and excellent electrocatalytic performance for water splitting in alkaline solution. Notably, the incorporation of Fe atoms on the electrolytic surface of binary transition-metal alloys improves water electrolysis's electrolytic activity in alkaline conditions. The free energy of adsorption of H$_2$ and O$_2$ molecules in the Fe sites is too low, providing high efficiency at low overpotential [28,29]. Tang et al. [29] performed

tests for HER in Fe$_{0.50}$Co$_{0.50}$P coatings, as well as computational calculations based on the density-functional theory (DFT). These authors showed that the incorporation of Fe sites reduces the free energy of H$_2$ adsorption onto the material surface. Furthermore, Friebel et al. [28] conducted experimental studies using X-ray absorption spectroscopy (XAS) and demonstrated that the Fe^{3+} species in Ni$_{1-x}$Fe$_x$OOH occupies octahedral sites with unusually short Fe–O bond distances. Moreover, computational calculations based on a density-functional theory with Hubbard U (DFT + U) methods revealed that the incorporation of Fe sites reduces the free energy from O$_2$ adsorption.

Electrodeposition is a simple and economically viable method to produce electrocatalytic materials, such as Fe-Ni coatings, because of its easy handling, low-cost, quick, and can be carried out at room temperature [22–24,26]. Generally, electrodeposition is performed in aqueous-based electroplating solutions; however, the narrow potential range related to the electrochemical water stability can affect the quality and adherence of the electrodeposited coating [30], since the water splitting occurs simultaneously with the electrodeposition of metals, such as Fe and Ni. Moreover, Fe^{2+} ions are unstable in an aqueous medium, requiring an electroplating bath with pH equal to or smaller than 3.5 [30] and/or the aid of complexing agents, such as cyanide, to minimize the precipitation of iron oxides/hydroxides. Besides, the occurrence of these reactions at low pH values results in low electrodeposition cathodic efficiency and increases the electrodeposited layer's stress [30]. Finally, the use of the complexing agents in aqueous electroplating formulations leads to the production of non-environmentally friendly wastewater.

Over the past decades, Deep Eutectic Solvents (DES) have proved to be an excellent alternative to aqueous-based electroplating solutions for the electrodeposition of metals and alloys [31–38], since they have excellent properties. Among them, it can be highlighted that they are easy to prepare, have good ionic conductivity, have high thermal stability, large electrochemical windows, and the metal salts have good solubility in DES [39,40]. Furthermore, the DES are biodegradable and non-toxic, which make them excellent environmentally friendly alternatives to formulate electroplating solutions to overcome the environmental problems associated with the non-environmental wastewater produced by the industrial electrodeposition process based on aqueous electroplating solutions [40,41]. The most widely studied eutectic mixtures are based on a combination of organic salts, such as choline chloride (ChCl), with hydrogen bond-donor compounds, such as either urea (U) or ethylene glycol (EG), in a molar ratio equal to 1:2 [41,42]. Yanai et al. [43] demonstrated that Fe-Ni alloy films could be successfully electrodeposited from a plating bath based on ChCl-EG with a molar ratio of 1:2.

Therefore, this study aimed to investigate the electrodeposition of Fe, Ni, and Fe$_x$Ni$_{(1-x)}$ ($0 \leq x \leq 1$) films on Cu substrates at 353.15 K using a mixture of ChCl and U in the molar ratio of 1:2 (1ChCl:2U) and without the addition of complexing agents. The effect of the molar ratio between Fe^{2+} and Ni^{2+} species in the bath composition was evaluated. Finally, the magnetic properties and electrocatalytic performance of the electrodeposited coatings for water electrolysis in alkaline solution were investigated.

2. Experimental procedure

2.1. Electrodeposition of the coatings

All chemicals were used as received. The Fe, Ni, and Fe$_x$Ni$_{(1-x)}$

coatings were electrodeposited on the Cu substrate from electroplating solutions prepared by the mixture of choline chloride (ChCl) (HOC$_2$H$_4$N (CH$_3$)$_3$Cl, Sigma-Aldrich, ≥ 98%) and urea (U) ((NH$_2$)$_2$CO, Sigma-Aldrich, ≥ 99%) in a molar ratio of 1:2 at 353.15 K and containing different molar ratios of iron chloride (FeCl$_2$4H$_2$O, Sigma-Aldrich ≥ 99%) and nickel chloride (NiCl$_2$6H$_2$O, Sigma-Aldrich ≥ 99%). The DES preparation followed the procedure described in the literature [41]. All electrochemical data were obtained by a potentiostat/galvanostat AUTO LAB PGSTAT30 (Metrohm-Eco Chemie) which was controlled by NOVA software version 2.1. All electrochemical measurements were performed in a conventional three-electrode cell of one compartment. Platinum plate (2 cm^2) and Ag(s)/AgCl(s) were the auxiliary and the reference

electrodes, respectively, for the experiments carried out in 1ChCl:2U. For cyclic voltammetric measurements, the working electrode was a Cu wire embedded in epoxy resin and a disk area of about 0.26 cm^2 was exposed. For the acquisition of the Mössbauer spectra and electronic scanning microscope images, all the coatings were electrodeposited on a Cu tape (1 cm^2 and thickness of 20 μm) supported on a glass plate. For the electrocatalytic tests, the coatings were electrodeposited on a Cu cylinder embedded in epoxy resin, and a disk area of about 2.04 cm^2 was exposed.

Before the electrodepositions, Cu wire and cylinder were mechanically polished with sandpaper from 100 up to 1200 mesh. Besides, the following cleaning procedure was applied to all Cu electrodes before the
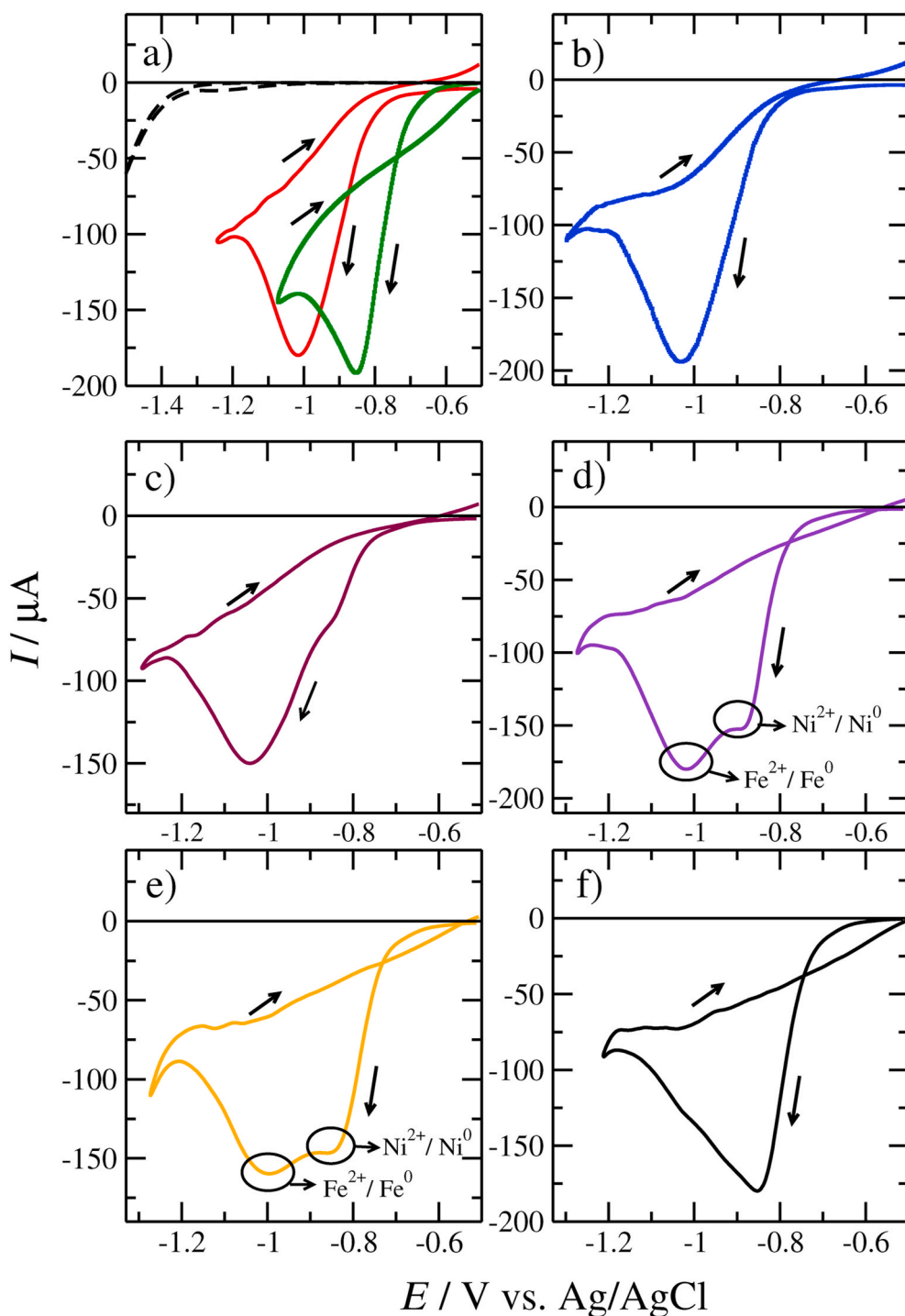

Fig. 1. Cyclic voltammograms obtained at different electroplating solutions: (a) 0.5 mol L^{-1} FeCl$_2$4H$_2$O (red line), 0.5 mol L^{-1} NiCl$_2$6H$_2$O (green line), and 1ChCl:2U solution, without adding metallic ions (dashed line), (b) 0.45 mol L^{-1} FeCl$_2$4H$_2$O + 0.05 mol L^{-1} NiCl$_2$6H$_2$O, (c) 0.35 mol L^{-1} FeCl$_2$4H$_2$O + 0.15 mol L^{-1} NiCl$_2$6H$_2$O, (d) 0.25 mol L^{-1} FeCl$_2$4H$_2$O + 0.25 mol L^{-1} NiCl$_2$6H$_2$O, (e) 0.15 mol L^{-1} FeCl$_2$4H$_2$O + 0.35 mol L^{-1} NiCl$_2$6H$_2$O, and (f) 0.05 mol L^{-1} FeCl$_2$4H$_2$O + 0.45 mol L^{-1} NiCl$_2$6H$_2$O, in electroplating solutions. Scan rate 10 mV s^{-1}. (For interpretation of the references to color in this figure legend, the reader is referred to the Web version of this article.)

coating depositions: degreasing in 10% NaOH solution, rinsing in Milli-Q water, pickling in 10% HCl solution, and, finally, rinsing again in Milli-Q water. The electrodepositions were performed under potentiostatic control for 30 min, at 353.15 K and at potentials selected from the cyclic voltammograms, which are shown in Fig. 1. All coatings were washed with water purified by the Milli-Q system to remove the solvent and then washed with isopropyl alcohol to remove the water adsorbed on the coating surfaces, and, finally, the sample was air-dried. The molar concentrations of the formulated electroplating solutions and the values applied to deposit the coatings are listed in Table 1.

2.2. Physical and chemical characterizations of the electrodeposited coatings

The surface morphologies of all electrodeposited coatings were analyzed using a high-resolution scanning electron microscope (FEG-SEM, model FEI-Quanta 450) operating at 20 kV coupled with Energy-dispersive X-ray spectroscopy (EDS). The X-ray diffraction (XRD) patterns of Fe, Ni, and $Fe_xNi_{(1-x)}$ coatings were collected using a PANalytical diffractometer, model XPertPRO equipped with Co-Kα radiation (λ = 0.1788 nm). The Inorganic Crystal Structure Database (ICSD) was used to identify the phases formed in the material. Chemical composition analyzes were performed in triplicate. The Fe, Ni, and $Fe_xNi_{(1-x)}$ coatings' magnetic properties were measured at room temperature in a vibrating sample magnetometer (VSM) Lakeshore 7400 with a maximum magnetic field amplitude of 7.5 kOe. The Mössbauer spectra were measured in a spectrometer SEE Co. model W302 in transmission mode using a radioactive ^{57}Co source diffused into a rhodium matrix. Mössbauer spectra were evaluated with the software package NORMOS, using the hyperfine field distribution method. Furthermore, metallic iron α-Fe was used for energy calibration, and references for isomer shifts (δ) are fitted concerning the α-Fe.

2.3. Electrocatalytic tests of $Fe_xNi_{(1-x)}$ coatings for water electrolysis

The electrochemically active surface areas (ECSA) for all Fe, Ni and Fe_xNi_{1-x} electrocatalysts were determined from the electrochemical double-layer capacitance (C_{dl}) of each electrocatalytic coating using Eq. (1) [44,45].

$$ECSA = \frac{C_{dl}}{C_s} \quad (1)$$

In this equation, C_S is the specific capacitance of a smooth and planar electrode per unit area, obtained at the same conditions as the working electrolyte. Although the ideal in such procedures is to produce smooth and planar electrodes of each catalytic material in which we want to measure C_S and calculate ECSA, this process is not practical for most electrodeposited materials [46]. However, the value of 0.040 mF cm^{-2} was used for Cs of Ni-based materials, based on typical reported values in aqueous NaOH solutions [11,46]. The C_{dl} values were determined from the cyclic voltammograms (CV) measured at different scan rates at an electrochemical window where there was no or minimal Faradaic activity, that is, in this potential region, it is assumed that all measured

currents are due to double-layer charging. Using the data of double-layer charging current (i_c) and scan rate (v), extracted from the cyclic voltammograms curves, we can calculate the C_{dl} from Eq. (2) [11,44–46].

$$i_c = vC_{dl} \quad (2)$$

According to Anantharaj et al. [47], this is the best method to determine the C_{dl} in electrocatalytic materials used for HER and OER, in which the i_c values were measured in the anodic and cathodic regions, and from then on, a plot resulting from the difference in double-layer charging current (Δi ($i_a - i_c$)) as a function of the scan rate will yield a linear line, the slope of which is C_{dl} of the investigated material.

The kinetic parameters of the Fe, Ni and $Fe_xNi_{(1-x)}$ coatings for the HER and OER were obtained by linear sweep voltammetry (LSV) at 1 mV s^{-1} in 0.5 mol L^{-1} NaOH at 298.15 K. However, all the measured potentials vs. $Hg_{(l)}|HgO_{(s)}|OH^-_{(aq)}$ were converted to the reversible hydrogen electrode (RHE) scale using Eq. (3) [48]. The equation referred to is an expression for the conversion of the potentials measured in the electrode from Hg/HgO to RHE that takes into account the pH value of the solution, that is, it can be used in various situations. This type of conversion is quite common in literature since the use of the RHE is not very convenient from an experimental point of view.

$$E_{vs.RHE} = E_{vs.\ Hg|HgO|OH} + 0.095 + 0.059\ pH \quad (3)$$

where $E_{vs.\ RHE}$ is the potential vs. RHE, and $E_{vs.\ Hg|HgO|OH}$ is the potential measured vs. $Hg_{(l)}|HgO_{(s)}|OH^-_{(aq)}$. Furthermore, in the water electrolysis process at 298.15 K, the equilibrium potential is −0.926 V vs. the standard hydrogen electrode (SHE) for HER [49] and 0.3033 V vs. SHE for OER [50]. The stabilities of all electrodeposited coatings for both HER and OER were evaluated in a long-term test for 120 h, at 298.15 K and applying 50 mA cm^{-2}.

3. Results and discussions

3.1. Cyclic voltammetry

Cyclic voltammetry experiments were carried out to investigate the electrochemical reduction of the Fe^{2+} and Ni^{2+} species on Cu substrate, as well as to determine the working potentials. Initially, the background scan of 1ChCl:2U solution in the absence of metal salts (dashed line) showed an excellent electrochemical window for electrodeposition between −0.5 and −1.2 V vs. Ag/AgCl, as can be seen in Fig. 1a. Likewise, the cyclic voltammograms obtained individually for 0.5 mol L^{-1} of $FeCl_24H_2O$ and $NiCl_26H_2O$ solutions, showed that the electrochemical reduction of Ni^{2+}/Ni^0 species occurs around −0.83 V vs. Ag/AgCl, while the reduction from Fe^{2+}/Fe^0 species occurs in more negative potentials around −1.0 V vs. Ag/AgCl. Moreover, the cyclic voltammograms obtained in electroplating solutions containing different ratios of Fe^{2+} and Ni^{2+} species are shown in Fig. 1(b-f). As the concentration of Ni^{2+} species increases in solution (≥ 0.25 mol L^{-1}), a second reduction peak is identified around −0.85 V vs. Ag/AgCl, which in turn is related to the electrochemical reduction of Ni^{2+}/Ni^0. The Fe, Ni, and $Fe_xNi_{(1-x)}$ coatings were prepared at the peak potentials identified in the cyclic

Table 1
Effect of the Fe^{2+}/Ni^{2+} ration in electroplating solution in the Fe/Ni ration in the electrodeposited coatings achieved at 353.15 K. The values of applied electrodeposition potentials are also displayed in this table.

Bath compositions		Fe^{2+}/Ni^{2+}	E_{peak}/V	Coatings composition by EDS		Fe/Ni	Sample label
$FeCl_2.4H_2O$/mol L^{-1}	$NiCl_2.6H_2O$/mol L^{-1}			Fe/at. %	Ni/at. %		
0.5	0		−1.00	100	0		Fe
0.45	0.05	9.00	−1.00	89 ± 1.8	11 ± 1.8	8.09	$Fe_{89}Ni_{11}$
0.35	0.15	2.33	−1.00	69 ± 1.3	31 ± 1.3	2.22	$Fe_{69}Ni_{31}$
0.25	0.25	1.00	−0.98	47 ± 1.9	53 ± 1.9	0.88	$Fe_{47}Ni_{53}$
0.15	0.35	0.43	−0.98	28 ± 2.2	72 ± 2.2	0.39	$Fe_{28}Ni_{72}$
0.05	0.45	0.11	−0.85	8 ± 1.5	92 ± 1.5	0.09	Fe_8Ni_{92}
0	0.5		−0.83	0	100		Ni

voltammograms, which are listed in Table 1. It is worth mentioning that there exists a current crossover-loop between forward and reverse sweep in the cyclic voltammograms recorded for 0.5 mol L^{-1} of $NiCl_26H_2O$ electrolyte. It is suggesting that Ni^{2+}/Ni^0 electrodeposition on the Cu electrode occurred via the nucleation-growth mechanism. On the other hand, this nucleation-growth controlled process is not observed in the cyclic voltammogram acquired for electrolyte containing 0.5 mol L^{-1} $FeCl_24H_2O$ ions only. This indicates that all electroactive sites on the substrate surface are covered during the electrodeposition. Furthermore, as the amounts of Ni^{2+} in the electrolytes increased, see Fig. 1(c-e), it is possible to observe the formation of a nucleation loop, indicating that an overpotential for nucleation and growth of the bulk alloy is required.

3.2. Morphological, chemical composition and structural characterization of the coatings

Fig. 2a shows the chemical composition of the $Fe_xNi_{(1-x)}$ electrodeposits obtained by EDS as a function of the molar concentration of Fe^{2+} species in the electroplating solutions. These results show that the percentage amount of Fe in the coatings is enhanced with increasing Fe^{2+} molar concentration. Analysing Table 1, it can be concluded that the Fe content in the electrodeposited coatings was always lower than the concentration of Fe^{2+} ions in the corresponding electroplating solutions. Therefore, the noblest metal, Ni, was preferentially electrodeposited, indicating that electrodeposition of the $Fe_xNi_{(1-x)}$ alloys in 1ChCl:2U eutectic mixture presented regular behavior.

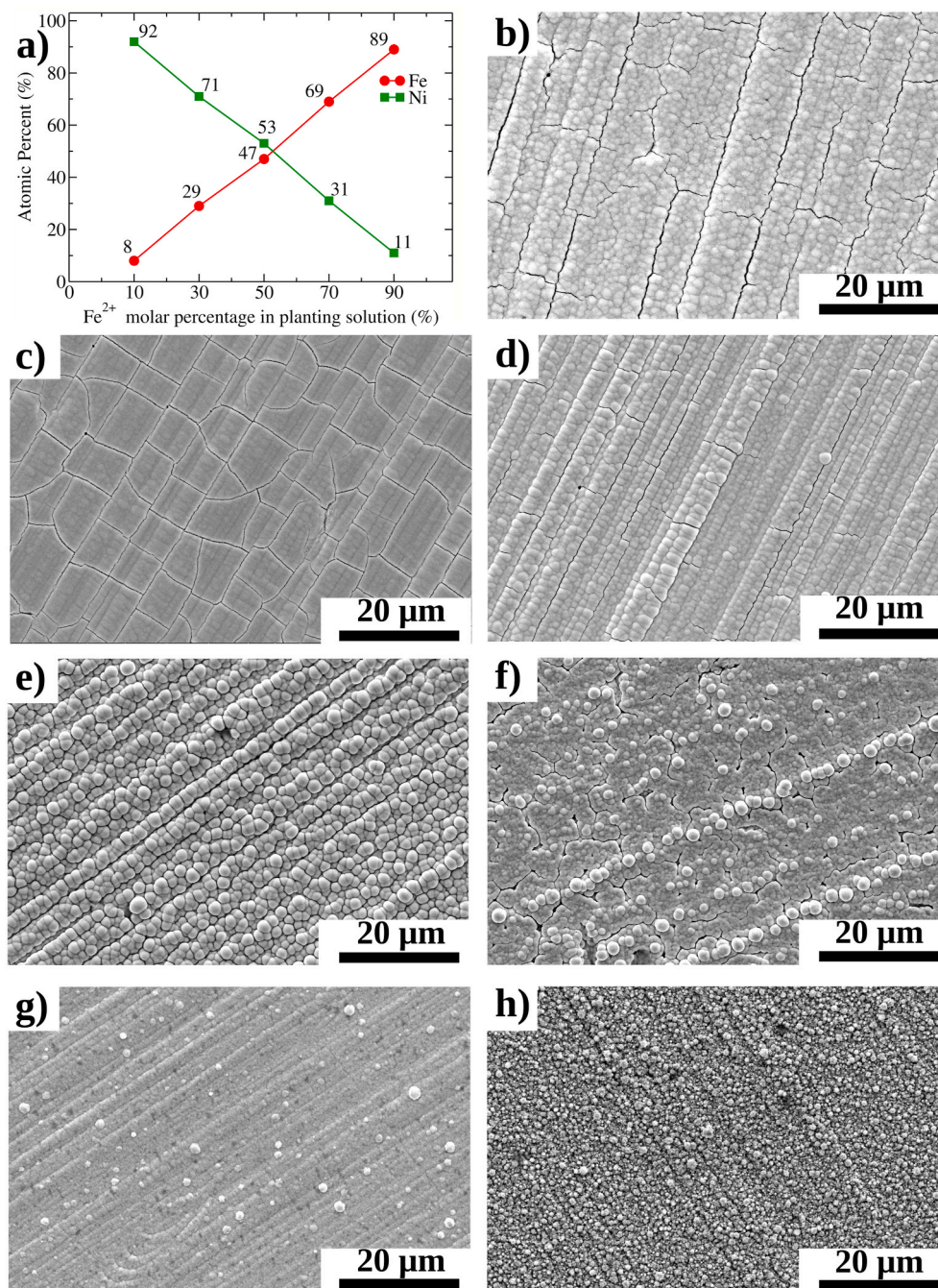**Fig. 2.** (a) Plot showing atomic weight percentage of Fe, Ni, and $Fe_xNi_{(1-x)}$ coatings with the bath composition. SEM images obtained for the electrodeposited coatings: (b) Fe, (c) $Fe_{89}Ni_{11}$, (d) $Fe_{69}Ni_{31}$, (e) $Fe_{47}Ni_{53}$, (f) $Fe_{28}Ni_{72}$, (g) Fe_8Ni_{92}, and (h) Ni.

The top surface morphologies of the electrodeposited coatings are shown in Fig. 2(b-h). The examination of the images revealed that the Fe-rich coatings, such as Fe, $Fe_{89}Ni_{11}$, and $Fe_{69}Ni_{31}$, are cracked as seen in Fig. 2(b-d), which is a typical morphology observed for Fe-rich alloys electrodeposited in both aqueous [51–53] and DES [43,54] electroplating solutions. Lammel et al. [55] and Eliaz et al. [56] attributed the formation of cracks on the top surface coatings to the high residual stress caused during the electrodeposition process, which may be due to the replacement of larger atoms by smaller atoms in the crystalline structure. Another possibility for the crack formation is due to the stress originated by gas bubbles formed during the electrochemical reduction of the solvent, since Vieira et al. [57] reported that when sufficiently negative potentials are applied, this leads to the electrochemical reduction of choline ions (Ch$^+$), hydroxyl groups of EG and ChCl, and/or trace of water present in DES.

On the other hand, for electrodeposits containing a high percentage of Ni, the top surface examination exposed a change to spherical agglomerates structures similar to the spherical particle morphology, which is usual for Fe-Ni coatings [52]. Besides, with the Ni enrichment of coatings, the spherical clusters' size decreased, as shown in Fig. 2(f-g). Furthermore, the Ni (Fig. 2h) coating was characterized by micronodules randomly distributed on the substrate surface, consistent with literature reports for Ni electrodeposits from DES [34–36].

Fig. 3 shows the XRD patterns achieved for Fe, Ni, and $Fe_xNi_{(1-x)}$ coatings. In all patterns, it is possible to identify peaks with angle 2θ at about 50 and 60°, which were indexed to the set of crystallographic planes {111} and {200}, respectively, being attributed to the face-centered cubic (fcc) structure of the Cu substrate (ICSD 52256 file card). However, no peak referring to the body-centered cubic phase (bcc) related to α-Fe was detected, probably due to the thin thickness of the coatings. Moreover, as the Ni content increased in the coatings, the width of the peak located in 2θ angle at about 53° increased, strongly
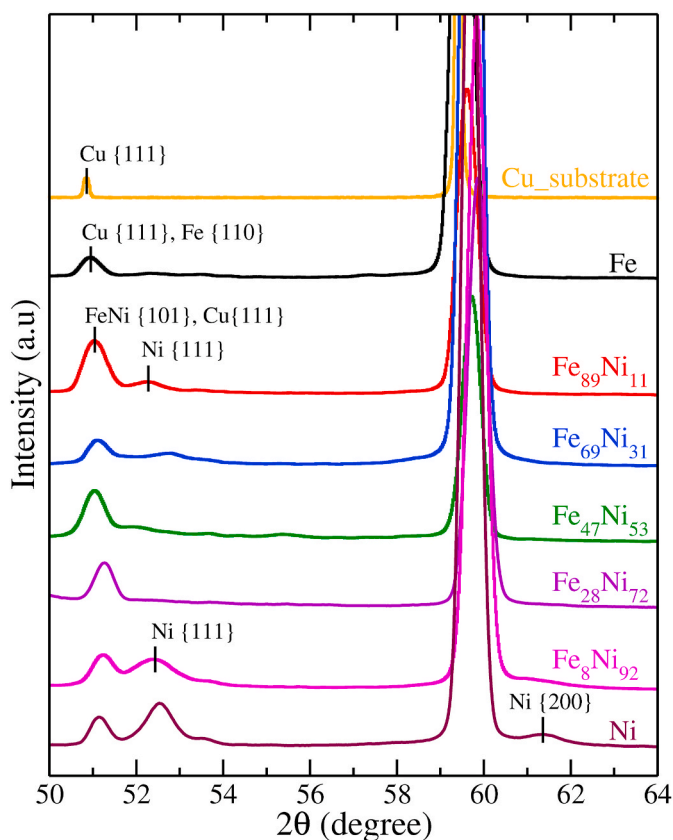

Fig. 3. XRD patterns of Fe, Ni, and $Fe_xNi_{(1-x)}$ coatings electrodeposited at different in electroplating solutions.

indicating the existence of an overlap of the fcc phases of Cu and bcc, attributed to the Fe-Ni alloy, according to ICSD 103555 file card. On the other hand, for Ni-rich coatings (Fe_8Ni_{92} and Ni), the XRD patterns revealed peaks at 2θ around 49, 52, and 61°, which can be indexed to {111} and {200}, from the fcc structure of Ni, according to the ICSD 43397 file card.

3.3. Mössbauer spectroscopy studies

Mössbauer spectroscopy is a useful technique for investigating iron sites and their chemical vicinity. Therefore, this technique was employed to confirm the formation of the Fe-Ni ferromagnetic phase, as well as to obtain the local magnetic texture parameters which are typical of ferromagnetic thin films [58].

Fig. 4(a-d) shows the room temperature Mössbauer spectra of coatings $Fe_{89}Ni_{11}$, $Fe_{69}Ni_{31}$, $Fe_{47}Ni_{53}$, and $Fe_{28}Ni_{72}$ along with the best fits of data, where all results were fitted by a distribution of the hyperfine magnetic field Fig. 4(e-h), indicating randomness of the environment where the Fe atoms are located [59]. Moreover, the values of the hyperfine parameters, isomer shift (δ), quadrupole shift (Δ), and hyperfine magnetic field (B_{hf}), are presented in Table 2. For the $Fe_{89}Ni_{11}$ coating (Fig. 4a), the Mössbauer spectra was fitted by a B_{hf} distribution, with the highest probability of B_{hf} centered on 34.6 T (see Fig. 4e). The growth of B_{hf} values in relation to α-Fe of 33.3 T are typical for Fe-Ni phase with lower Ni concentration. According to Johnson et al. [60], the Fe-Ni alloy with a concentration of Ni less than 25% maintains the bcc structure α-Fe, and the B_{hf} around the ^{57}Fe atom grew by 0.76 T for each Ni atom that substitutes the Fe atom in one of on the vertices of the bcc structure α-Fe [61]. However, when the Ni concentration was greater than 30%, such as $Fe_{69}Ni_{31}$, $Fe_{47}Ni_{53}$, and $Fe_{28}Ni_{72}$, the Mössbauer spectra showed B_{hf} distributions centered on 33.1, 31.0, and 28.7 T, respectively. The reduction of the hyperfine magnetic field in relation to the α-Fe of 33.3 T is due to the formation of a new atomically disordered magnetic phase, which began to form around Ni concentrations higher than 28%, as explained by Johnson et al. [60]. The value of 33.1 T for the $Fe_{69}Ni_{31}$ spectrum indicated the beginning of the formation of the disordered magnetic phase in which the disorder caused by the incorporation of Ni atoms is still too low that it maintains the bcc structure α–Fe. Besides, the distributions of B_{hf} centered on 31.0, and 28.7 T were similar to those values reported in the literature for chemically disordered taenite phase in the Fe-Ni alloy [62–65], generally formed in compositions around $Fe_{50}Ni_{50}$, as reported by Abdu et al. [65]. Therefore, we can assign these distributions of B_{hf} to the chemically disordered Fe-Ni taenite phase, characterizing the formation of the Ni-rich Fe-Ni alloy in the coatings $Fe_{47}Ni_{53}$ and $Fe_{28}Ni_{72}$.

However, for the $Fe_{89}Ni_{11}$ and $Fe_{69}Ni_{31}$ coatings, Mössbauer spectra showed the paramagnetic contribution is a singlet, with δ = 0.01 and 0.10 mm s^{-1}, respectively, indicating the location of Fe atoms in an fcc structure [59]. Such behavior originates from the diffusion of Fe atoms to the Cu substrate's fcc structure during electrodeposition, thus forming a Cu-Fe (Fe in the Cu matrix) solid-solution. Despite the coating becoming Ni-richer, the singlet contribution was suppressed. A similar investigation conducted by our research group with Fe-Co coatings [66] revealed that the pure Fe coating electrodeposited under identical conditions presented a well-defined singlet contribution attributed to Fe-Cu solid-solution. Furthermore, it is interesting to note that the values of δ of the distribution calculated for all sub-spectra in relation to α-Fe were in the range of 0.01 at 0.11 mm s^{-1}, and the values of Δ were quite close to zero. These values were compatible with those calculated by Kozlovskiy et al. [61] for Fe-Ni alloy electrodeposited from aqueous electrolytes. Furthermore, the location of the B_{hf} in the range of 28.7–37.0 T indicates that in the $Fe_xNi_{(1-x)}$ coatings, the formation of magnetically ordered iron oxides did not occur, which is easily formed in aqueous systems due to the low pH values of the electroplating solution.

Moreover, we would like to highlight an important point observed in the $Fe_{89}Ni_{11}$ and $Fe_{69}Ni_{31}$ coatings: irregularity in the intensities of
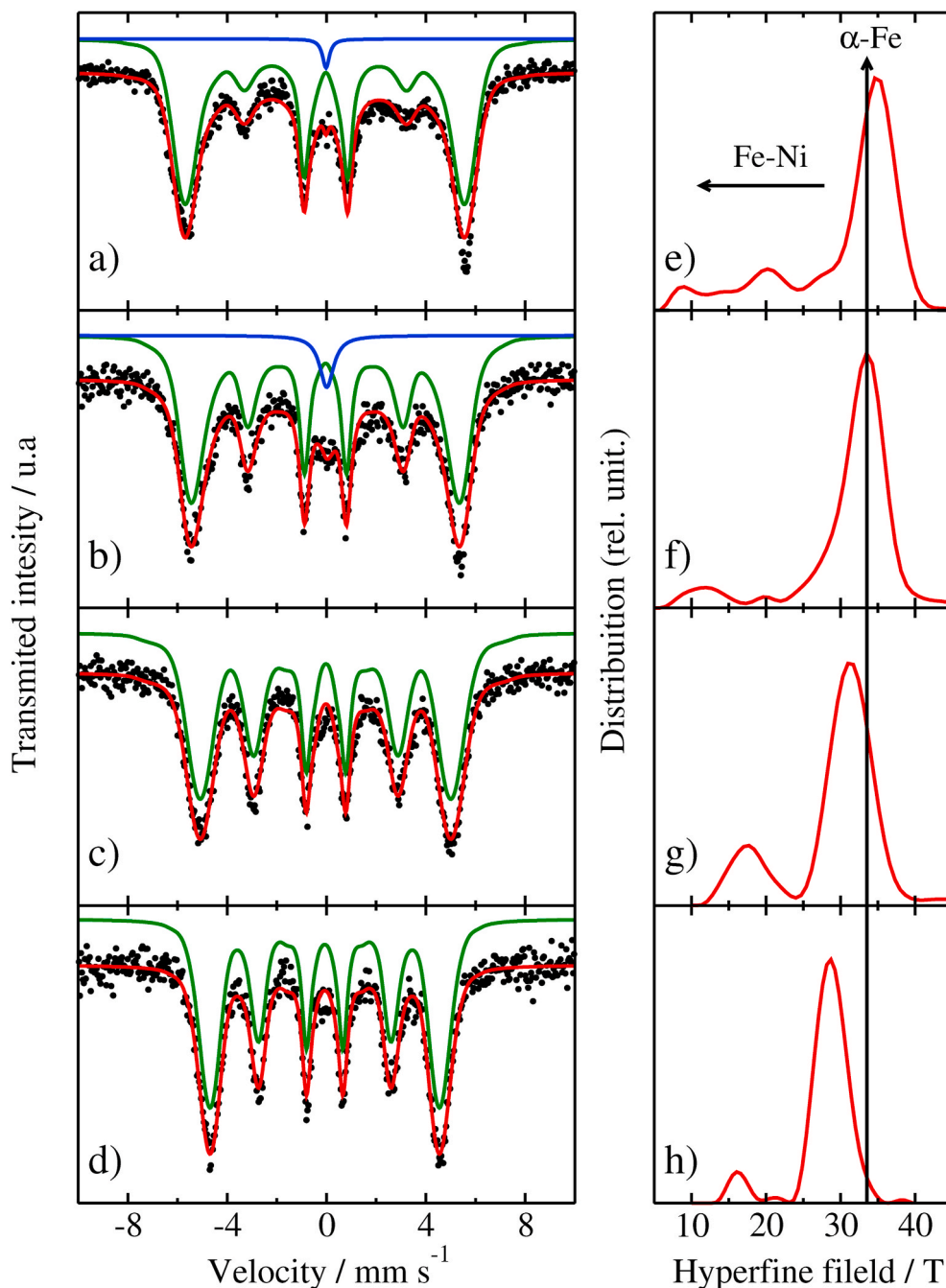
Fig. 4. Mössbauer spectra of (a) $Fe_{89}Ni_{11}$, (b) $Fe_{69}Ni_{31}$, (c) $Fe_{47}Ni_{53}$ e (d) $Fe_{28}Ni_{72}$ coatings. Hyperfine field distribution of (e) $Fe_{89}Ni_{11}$, (f) $Fe_{69}Ni_{31}$, (g) $Fe_{47}Ni_{53}$ e (h) $Fe_{28}Ni_{72}$ coatings.

Table 2
Parameters Mössbauer of $Fe_xNi_{(1-x)}$ coatings obtained from hyperfine fits.

Sample	Mössbauer parameters					
	Fitting	B_{hf} (max)/ T	δ/mm s^{-1}	Δ/mm s^{-1}	$I_{2.5}/$ $I_{1.6}$	θ^0
$Fe_{89}Ni_{11}$	Distribution	34.6	0.06	0.03	0.06	17.8
	Singlet		0.02			
$Fe_{69}Ni_{31}$	Distribution	33.1	0.07	0.01	0.33	39.1
	Singlet		0.19			
$Fe_{47}Ni_{53}$	Distribution	31.0	0.09	0.02	0.35	40.0
$Fe_{28}Ni_{72}$	Distribution	28.7	0.04	0.01	0.38	42.1

absorption lines two and five observed in the Zeeman sextet in the Mössbauer spectra of ^{57}Fe nuclei. This region of the spectrum carries information about magnetic moments' orientation [67]. The magnetic texture (preferred orientations) in ferromagnetic materials by Mössbauer spectroscopy is determined by the ratio of intensities of the second and fifth lines to the first and sixth resonance lines, which depends on the angle (θ) between the incidence direction of the gamma-rays beam and the orientation of the hyperfine magnetic field: $I_{2.5}/I_{1.6} = 4sin^2\theta/3(1 + cos^2\theta)$. The ratio of intensities of the coatings studied (see Table 2) suggested the existence of a magnetic texture, with the magnetic moments oriented in the same direction as the axis of propagation in the gamma-rays. However, the fitting revealed that only the sub-spectra referring to the bcc structure α-Fe presented a relevant magnetic texture. The other sextets related to $Fe_{47}Ni_{53}$ and $Fe_{28}Ni_{72}$

coatings presented a low degree of orientation reflected in the θ values shown in Table 2; such results can be explained by the presence of a chemically disordered taenite phase which directly influences the ordering of the magnetic domains of the coatings.

3.4. Magnetic properties

The magnetic properties of the Fe, Ni, and $Fe_xNi_{(1-x)}$ coatings were investigated by analysis of magnetic hysteresis loops using a vibrant sample magnetometer operating at room temperature, as shown in Fig. 5. The experimental results revealed well-defined magnetic hysteresis loops and ferromagnetic behavior in all coatings. Moreover, in all analyzed samples, the magnetic hysteresis loops showed a low value of the coercive field (H_c). The coercivity of coatings Fe, $Fe_{89}Ni_{11}$, $Fe_{69}Ni_{31}$, $Fe_{47}Ni_{53}$, $Fe_{28}Ni_{72}$, Fe_8Ni_{92}, and Ni was around 328, 292, 185, 126, 83, 92, and 125 Oe, respectively. Such results suggested that the coatings were soft magnetic materials, typical of Fe and Ni-based electrodeposits [22]. Therefore, the electrodeposition of Fe and Ni-based coatings from 1ChCl:2U eutectic solvent preserved the magnetic properties observed in aqueous solutions [68,69].

Analyzing the hysteresis loops in detail, it was possible to identify a relationship between the H_c value and the Ni concentration in the coatings. Fig. 6 shows the H_c values dependence with the electrodeposited Ni concentration. Since the concentration of Ni increased, the
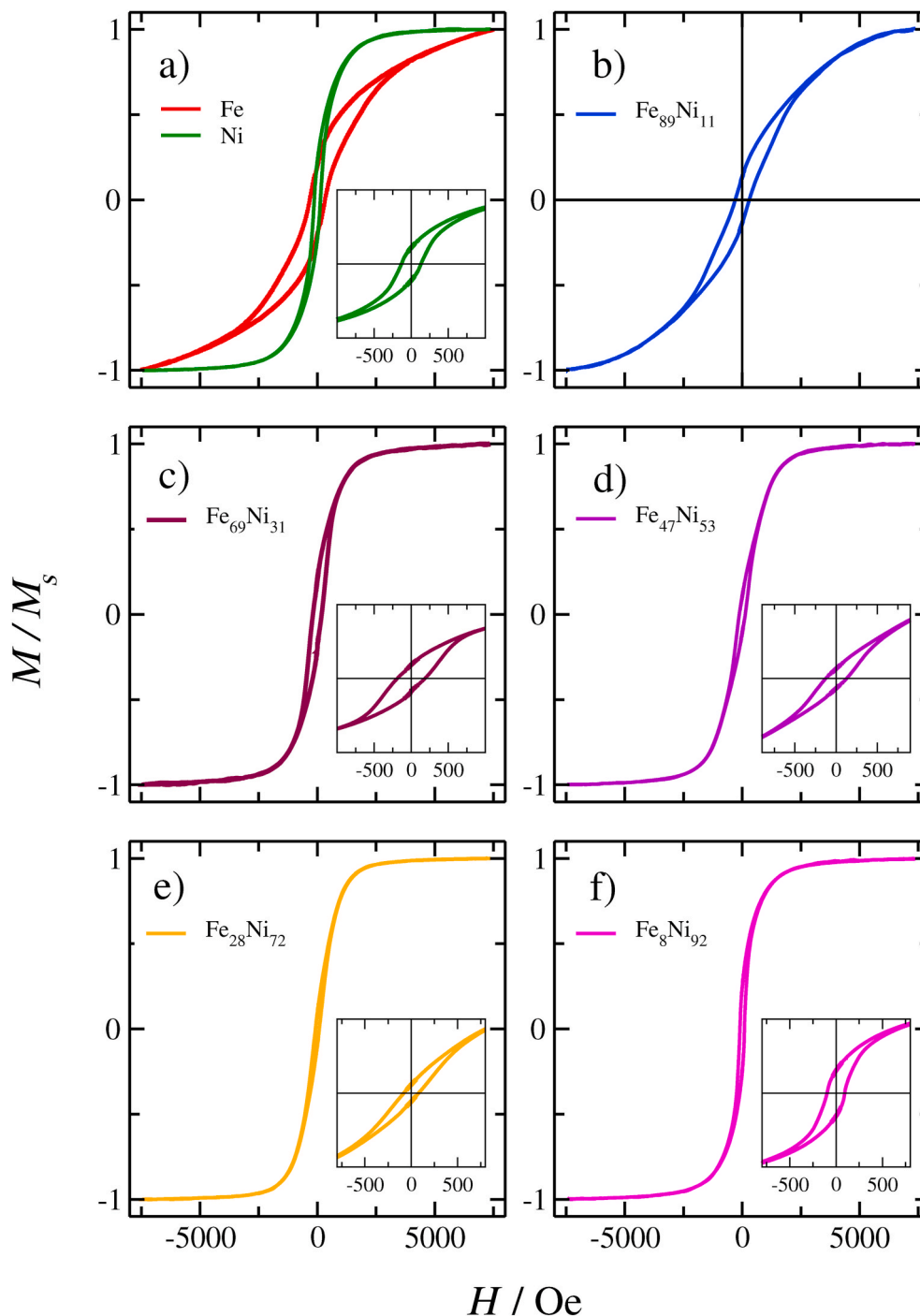

Fig. 5. Magnetization curves of the Fe, Ni, and $Fe_xNi_{(1-x)}$ electrodeposited (a-f). Inset (a-f): magnification of curves for the analysis of the magnetic hysteresis.
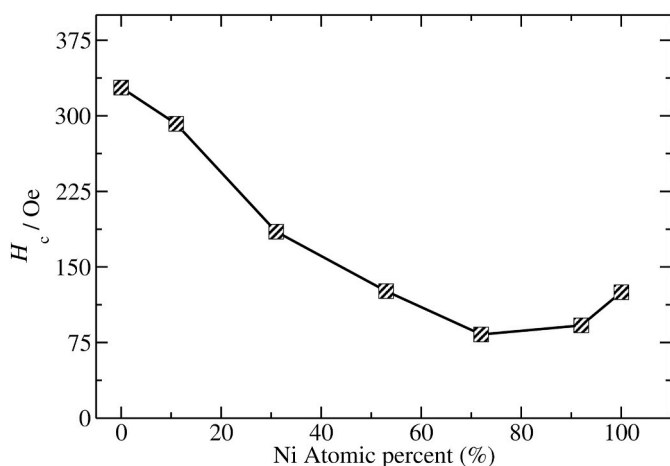
Fig. 6. Relationship between coercivity H_c and Ni content in the $Fe_xNi_{(1-x)}$ coatings.

value of H_c decreased. Thus, the additional increase in Ni content caused significant changes in the coercivity of the $Fe_xNi_{(1-x)}$ electrodeposits. This behavior can be correlated to the formation process of the $Fe_xNi_{(1-x)}$ alloy by the incorporation of Ni atoms into the crystalline structure of the electrodeposits. This process promoted a significant number of defects in the crystalline structure of the material, resulting in changes of the ordering of the magnetic domains and increasing the hysteresis losses [69]. Based on this result, allying with XRD and Mössbauer spectroscopy analyses, it was possible to attest the incorporation of Ni into the structure of the coatings.

3.5. Electrocatalytic properties for water splitting

The ECSA data for Fe_xNi_{1-x} electrocatalysts were estimated from cyclic voltammograms obtained at different scan rates, as shown in Fig. S1, S3 and S4 in supplementary material, as well as ECSA values, which are listed in Table 3. The results showed that the Fe and $Fe_{89}Ni_{11}$ electrocatalysts exhibit the highest ECSA values among all the investigated materials with 111.2 and 58.1 cm^2, respectively. The high ECSA values for these electrocatalysts is related to the cracked morphology, which provides a high surface area of exposure for both materials. When comparing the ECSA results with the surface morphologies of all Fe_xNi_{1-x} coatings (see Fig. 2), it is possible to observe that the addition of Ni

Table 3
Comparison electrocatalytic activity for HER of electrocatalysts Fe, Ni and $Fe_xNi_{(1-x)}$ 0.5 mol L^{-1} NaOH at 298.15 K with some recently reported electrocatalysts in alkaline solution.

Electrocatalysts	ECSA/ cm^{-2}	b/mV dec^{-1}	$J_{0\,(ECSA)}$/ mA cm^{-2}	η/mV at 10 mA cm^{-2}	Reference
Ni	21.3	140.1	1.1	301	This work
Fe_8Ni_{92}	27.2	105.0	0.4	256	This work
$Fe_{28}Ni_{62}$	42.2	134.7	1.4	236	This work
$Fe_{47}Ni_{53}$	43.5	136.8	1.9	220	This work
$Fe_{69}Ni_{31}$	37.7	150.8	3.6	191	This work
$Fe_{89}Ni_{11}$	58.1	124.5	2.9	152	This work
Fe	111.2	74.4	1.4	111	This work
Ni-Fe-P		84		142	[71]
FeNi-P		82		102	[27]
FeNi-S/NF		77		47	[25]
MoS2-Ni3S2		61		98	[72]
NiFe		112		139	[26]
CoP/CC		55		103	[29]
Fe1.0Co1.1Ni1.4NC		168		175	[48]
NiFe2O4		60		201	[20]

content in the coatings reduces the crack density, indicating that such morphology is directly related to the Fe content present in the coating. Therefore, this particular behavior correlates with the ECSA results, since it presents a reduction trend with Ni, ranging from 111.2 to 21.3 cm^2 for the coatings which are composed of 100% of Fe and Ni, respectively. Furthermore, all materials studied presented ECSA values much higher than their geometric areas of 2 cm^2. This result indicates that the electrodeposited Fe_xNi_{1-x} coatings have a large number of active sites exposed for both HER and OER.

The process of the electrochemical water splitting implies the breaking down of water molecules into hydrogen and oxygen, with HER occurring on the cathode, whereas the OER takes place on the anode [6]. Cathodic polarization by LSV was used to evaluate the electrocatalytic activity of Fe, Ni, and $Fe_xNi_{(1-x)}$ coatings for HER in 0.5 mol L^{-1} NaOH. From a practical point of view, when thinking about an industrial application, energy consumption is an important parameter to be evaluated in the process of water splitting. In this sense, the overpotential value necessary to deliver at a current density per geometric area of 10 mAcm^{-2} is the most widely used criterion to classify the performance of electrocatalysts, since the value of 10 mAcm^{-2} corresponds to the working current density for a solar water-splitting device with an efficiency of 2.3 % [6,70]. However, in this situation, the electrocatalytic effects are mixed with surface roughness effects and the results do not represent the true electrocatalytic activity of the material. To overcome this problem, the LSV curves used for the Tafel plot were normalized by the corresponding ECSA.

Fig. 7a shows the polarization curves for the Fe, Ni, and $Fe_xNi_{(1-x)}$ coatings recorded at 298.15 K. The values of the overpotentials required for providing a current density of 10 mA cm^{-2} (geometric area) for Ni, Fe_8Ni_{92}, $Fe_{28}Ni_{72}$, $Fe_{47}Ni_{53}$, $Fe_{69}Ni_{31}$, $Fe_{89}Ni_{11}$, and Fe coatings are listed in Table 3. Of note, that the Fe and $Fe_{89}Ni_{11}$ electrocatalysts showed an excellent HER performance since the overpotential values in these materials are comparable or lower to some non-precious metal catalysts already studied in the literature, as shown in Table 3. Here, the increase of Fe content in these binary alloys caused a decrease in the overpotential values, indicating that the incorporation of Fe into the coating improved the electrocatalytic activity of the material. According to Shang et al. [25], the Fe incorporating bimetallic Fe-Ni alloys increased active sites for water splitting. The authors showed that the insert of Fe in the binary alloy improved the properties of HER; furthermore, the coating with Fe:Ni 3:1 M ratio presented the high electrochemical activity and excellent stability for overall water electrolysis. Moreover, the free energy change for hydrogen adsorption on the catalyst surface is the parameter used to quantify the hydrogen-metal bond strength. For instance, Tang et al. [29] performed computational calculations based on quantum-mechanical theory and concluded that the free energy for the hydrogen adsorption on $Fe_{0.50}Co_{0.50}P$ was less negative than one calculated for the CoP electrocatalyst, revealing that the incorporation of Fe sites reduces the free energy of H_2 adsorption onto the material surface. Therefore, the iron inserted in the electrocatalyst material improved its performance for HER.

The linear fitting of the LSV cathodic curves by the Tafel equation ($\eta = a + b \cdot log(J)$) allowed the calculation of the kinetic parameters for the HER. In alkaline medium, HER is described by three mechanisms: Volmer-Tafel, Volmer-Heyrovsky, and Volmer, corresponding to slope values of 30, 40, and 120 mV dec^{-1} [3], respectively. The Tafel plots for the Fe_xNi_{1-x} electrocatalysts normalized by their respective ECSAs are presented in Fig. 7b, while the electrocatalytic data of the Tafel slope and exchange current density ($J_{0(ECSA)}$) are listed in Table 3. For the Fe electrocatalyst, the corresponding Tafel slope is 74.4 mV dec^{-1}, suggesting that HER was mainly controlled by the Volmer-Heyrovsky mechanism with the determining step being the Heyrovsky reaction. However, as the chemical composition of Ni increases in the electrocatalysts, the Tafel slopes suffered a significant increase reaching 124.5 mV dec^{-1} for $Fe_{89}Ni_{11}$. Also, for the other $Fe_xNi_{(1-x)}$ and Ni electrocatalysts, the values were higher, indicating that the Volmer reaction
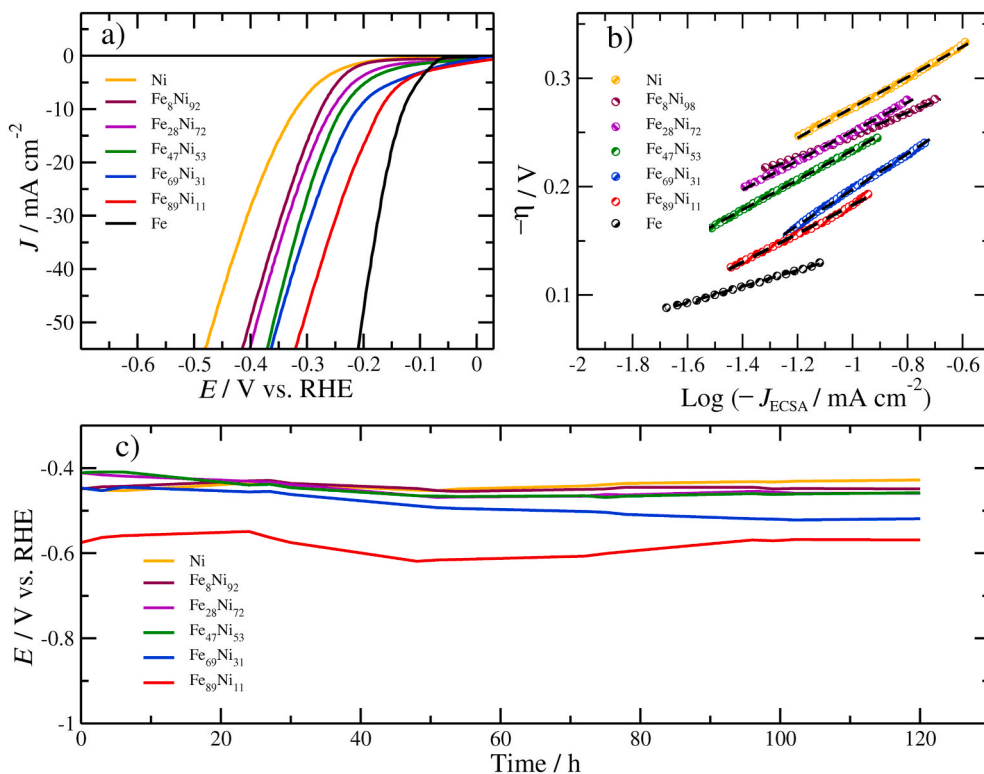
Fig. 7. (a) The polarization curves for HER on Fe, Ni, and $Fe_xNi_{(1-x)}$ electrocatalysts, normalized by geometric area. (b) Tafel slope with linear fitting, normalized by ECSA. (c) Stability tests in continuous operation at 50 mA cm^{-2} for 120 h, normalized by geometric area.

was the determining step for HER. These results showed that the Fe and Ni sites are active for HER. However, the effect of the decreasing of the slope value for Fe-rich electrocatalysts suggested that the HER kinetics

on the Fe sites was faster and, therefore, the electrocatalytic activity of Fe-Ni coatings was improved with the addition of Fe. The $Fe_{69}Ni_{31}$ coating presented the highest value of $J_{0(ECSA)}$ of 3.6 mA cm^{-2},

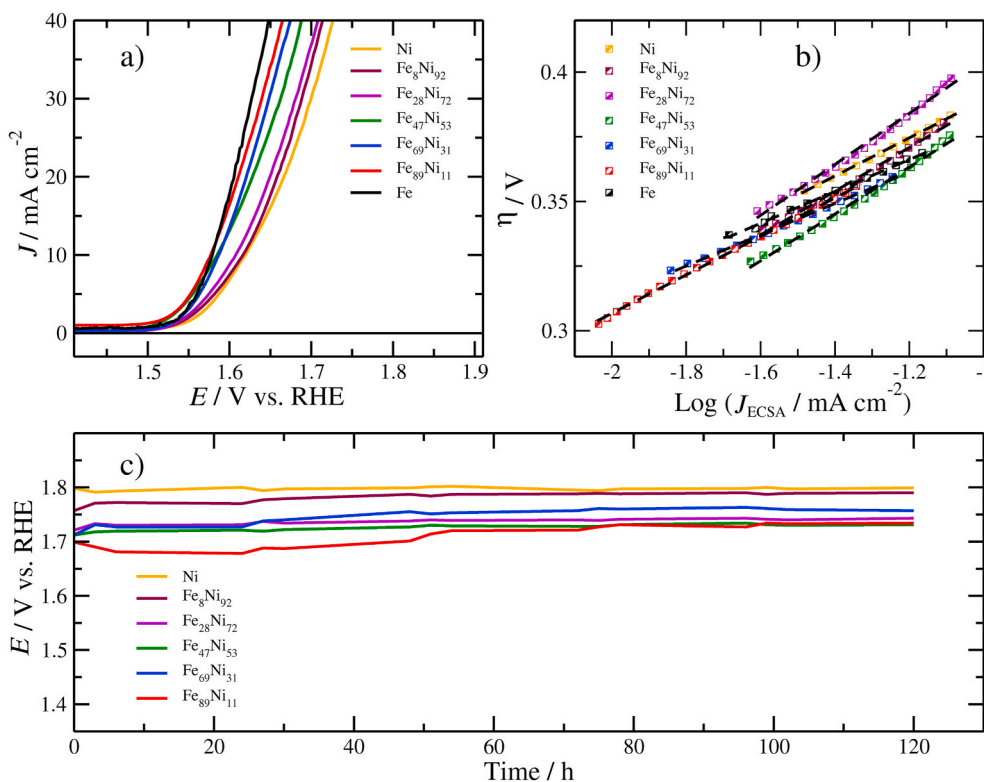**Fig. 8.** (a) The polarization curves for OER on Fe, Ni, and $Fe_xNi_{(1-x)}$ electrocatalysts, normalized by geometric area. (b) Tafel slope with linear fitting, normalized by ECSA. (c) Stability tests in continuous operation at 50 mA cm^{-2} for 120 h, normalized by geometric area.

indicating the highest charge transfer kinetics for the HER. In Table 3, it was possible to analyze the electrochemical parameters for all investigated electrocatalysts. Such results were comparable and sometimes superior to the other transition metals based electrocatalysts previously reported in the literature, as shown in Table 3.

The stability tests of the electrocatalysts for HER were investigated by continuous operation in which electrocatalysts were subjected to a current density of 50 mA cm^{-2} for 120 h, as can be seen in Fig. 7c. During the tests, the nucleation of H$_2$ gas bubbles on the Fe coating surface caused its detachment from the substrate. On the other hand, Ni, Fe$_8$Ni$_{92}$, Fe$_{28}$Ni$_{72}$, Fe$_{47}$Ni$_{53}$, Fe$_{69}$Ni$_{31}$, and Fe$_{89}$Ni$_{11}$ showed excellent physical and electrocatalytic stability, keeping the potential values stable throughout the continuous operation, indicating that this property makes them promising electrocatalysts materials for the hydrogen production of HER on a large scale.

Subsequently, the electrocatalytic performance of the coatings Fe, Ni, and Fe$_x$Ni$_{(1-x)}$ for OER was also investigated. Fig. 8a shows the anodic polarization curves obtained in 0.5 mol L^{-1} NaOH at 298.15 K. The values of the overpotential required for providing a current density of 10 mA cm^{-2} (geometric area) of the electrocatalytic coatings Ni, Fe$_8$Ni$_{92}$, Fe$_{28}$Ni$_{72}$, Fe$_{47}$Ni$_{53}$, Fe$_{69}$Ni$_{31}$, Fe$_{89}$Ni$_{11}$, and Fe are listed in Table 4. Among them, the Fe$_{89}$Ni$_{11}$ catalyst presented the highest performance for OER, since a small overpotential of only 367 mV was needed to provide a current density of 10 mA cm^{-2} (geometric area). The incorporation of Fe in Fe$_x$Ni$_{(1-x)}$ metallic coatings promoted the enhancement of electrocatalytic performance. The comparison among the values obtained here and the values published in the literature are shown in Table 4. Previous studies have reported the presence of a shoulder in the anodic sweep because of the oxidation of Ni^{2+} to Ni^{3+} in Ni-Fe coatings. This electrochemical process is well-known owing to the formation of nickel hydroxide/oxyhydroxide during the oxygen evolution reaction on Ni-Fe alloys top surface in alkaline media [73]. This oxidation peak was not detected, as can be seen in Fig. 8a. However, the presence of Fe in higher amounts in the Ni-Fe coatings could shift the Ni^{2+}/Ni^{3+} oxidation peaks to higher potential regions, therefore, this oxidation process becomes less pronounced and even overlaps with the rapidly increasing OER current [21,74,75]. Furthermore, Friebel et al. [28] conducted an experimental study based on XAS to show that Fe^{3+} in Ni$_{1-x}$Fe$_x$OOH occupies octahedral sites with unusually short Fe–O bond distances, induced by edge-sharing with surrounding [NiO$_6$] octahedra. Additionally, these researchers performed density functional calculations to explain that this structural arrangement results in near optimal adsorption energies of OER intermediates and low overpotentials at Fe sites, in contrast to Ni sites for water electrolysis, revealing that the incorporation of Fe sites reduces the free energy from

O$_2$ adsorption.

Fig. 8b displays the Tafel plots of all Fe$_x$Ni$_{1-x}$ electrocatalysts in which the current values were normalized by their respective ECSAs. The electrocatalytic data obtained from Tafel fits for OER are listed in Table 4. Fe$_{47}$Ni$_{53}$ and Fe$_{28}$Ni$_{62}$ electrocatalysts possess the best OER electrocatalytic activity among the others, with J$_{0(ECSA)}$ of 5.9×10^{-3} and $7.9\ 7 \times 10^{-3}$ mA cm^{-2}, respectively, indicating the fastest charge transfer kinetics compared to the others. Although it is rather difficult to define the OER mechanism using the Tafel slope [76], these results were obtained in order to compare with other electrocatalysts already studied in the literature as shown in Table 4. The results show that the Fe$_x$Ni$_{(1-x)}$ electrocatalysts showed the lowest Tafel slope in some situations, indicating greater efficiency of these coatings for OER in alkaline medium. Therefore, the Fe$_x$Ni$_{(1-x)}$ based electrocatalysts prepared in 1ChCl:2U presented an excellent electrocatalytic performance for both HER and OER, suggesting that the material has many active sites for both cases. Furthermore, the stability of the coatings in continuous operation has been investigated at 50 mA cm^{-2} for 120 h, as shown in Fig. 8c. Again, the Fe coating detached from the Cu substrate during continuous operation for electrochemical water splitting. However, the other coatings proved to be stable without significant changes in potential values, which indicates excellent stability for OER. Thus, the remarkable stability for HER and OER was related to the structural characteristics of the Fe$_x$Ni$_{(1-x)}$ coatings as well as excellent adhesion to the Cu substrate, as already reported by Shujuan Wang et al. [36]. In addition, according to O'Brien et al. [77], the incorporation of Ni in the alloy structure provides to the material an improvement in its corrosion resistance in concentrated alkaline solutions. Such characteristics are fundamental for the excellent performance of the electrocatalysts used in the electrochemical water splitting, indicating favorable perspectives for industrial-scale applications.

4. Conclusions

The Fe, Ni, and Fe$_x$Ni$_{(1-x)}$ coatings were successfully electrodeposited on Cu surfaces from a eutectic mixture of choline chloride-urea without the necessity of add additives. The Mössbauer and XRD analyses revealed that the Fe-Ni phase was formed only in the coatings Fe$_{89}$Ni$_{11}$, Fe$_{69}$Ni$_{31}$, Fe$_{47}$Ni$_{53}$, and Fe$_{28}$Ni$_{72}$. The Fe$_x$Ni$_{(1-x)}$ coatings were characterized as soft magnetic materials. The electrocatalytic assays demonstrated that Fe, Ni, and Fe$_x$Ni$_{(1-x)}$ coatings had good electrocatalytic performance for electrochemical water splitting in 0.5 mol L^{-1} NaOH solution. Among them, the Fe$_{69}$Ni$_{31}$ electrocatalyst displayed the highest electrocatalytic performance for HER, while the coatings Fe$_{47}$Ni$_{53}$ and Fe$_{28}$Ni$_{62}$ presented a significant increase in the electrocatalytic activity for OER. Fe coating did not present mechanical stability during gas evolution in both HER and OER in continuous operation for 120 h with a current density of 50 mA cm^{-2}. In contrast, all Fe$_x$Ni$_{(1-x)}$ and Ni electrocatalysts remained stable during the 120 h of the long-term tests. Finally, Deep Eutectic Solvents from choline chloride-urea provide a new strategy for electrodeposition of Fe and Ni electrocatalysts used as environmentally friendly electroplating solutions.

Table 4
Comparison electrocatalytic activity for OER of electrocatalysts Fe, Ni and Fe$_x$Ni$_{(1-x)}$ 0.5 mol L^{-1} NaOH at 298.15 K with several recently reported electrocatalysts in alkaline solution.

Electrocatalysts	b/mV dec^{-1}	$J_{0\ (ECSA)}$/mA cm^{-2}	η/mV at 10 mA cm^{-2}	Reference
Ni	73.6	4.9×10^{-4}	409	This work
Fe$_8$Ni$_{92}$	84.4	2.5×10^{-3}	406	This work
Fe$_{28}$Ni$_{62}$	98.5	7.9×10^{-3}	398	This work
Fe$_{47}$Ni$_{53}$	90.5	5.9×10^{-3}	374	This work
Fe$_{69}$Ni$_{31}$	60.4	2.1×10^{-4}	377	This work
Fe$_{89}$Ni$_{11}$	74.3	8.8×10^{-4}	367	This work
Fe	61.5	2.7×10^{-4}	370	This work
FeNi-P	72		224	[27]
Fe1.0Co1.1Ni1.4NC	60		270	[48]
CoCr LDH	81		340	[78]
Ni-Co-S/Cu	109		363	[79]
Co$_{0.13}$Ni$_{0.87}$Se$_2$/Ti	94		320	[80]
MnO$_2$/Ti	241		408	[15]
CoP$_3$/Ti	276		322	[15]

CRediT authorship contribution statement

Francisco G.S. Oliveira: Investigation, Conceptualization, Methodology, Writing – original draft. **Luis P.M. Santos:** Writing – original draft, Conceptualization, Methodology. **Rodolfo B. da Silva:** Writing – original draft, Magnetic properties methodology. **Marcio A. Correa:** Writing – original draft, Investigation, Magnetic properties methodology. **Felipe Bohn:** Writing – original draft, Magnetic properties methodology. **Adriana N. Correia:** Project administration, Supervision. **Luciana Vieira:** Writing – original draft, Conceptualization. **Igor F. Vasconcelos:** Writing – review & editing, Supervision. **Pedro de Lima-Neto:** Project administration, Writing – review & editing, Supervision, Conceptualization, Methodology.

Declaration of competing interest

The authors declare that they have no known competing financial interests or personal relationships that could have appeared to influence the work reported in this paper.

Acknowledgements

Appendix A. Supplementary data

Supplementary data to this article can be found online at https://doi.org/10.1016/j.matchemphys.2022.125738.

References

[1] IPCC, Global Warming of 1.5 °C. An IPCC Special Report on the impacts of global warming of 1.5 °C above pre-industrial levels and related global greenhouse gas emission pathways, in: V. Masson-Delmotte, P. Zhai, H.O. Pörtner, D. Roberts, J. Skea, P.R. Shukla, A. Pirani, W. Moufouma-Okia, C. Péan, R. Pidcock, S. Connors, J.B.R. Matthews, Y. Chen, X. Zhou, M.I. Gomis, E. Lonnoy, T. Maycock, M. Tignor, T. Waterfield (Eds.), The Context of Strengthening the Global Response to the Threat of Climate Change, Sustainable Development, and Efforts to Eradicate Poverty, In Press, 2018.
[2] IPCC, in: B. Metz, O.R. Davidson, P.R. Bosch, R. Dave, L.A. Meyer (Eds.), Climate Change 2007: Mitigation. Contribution of Working Group III to the Fourth Assessment Report of the Intergovernmental Panel on Climate Change, Cambridge University Press, Cambridge, United Kingdom and New York, NY, 2007, 2007.
[3] J. Wang, F. Xu, H. Jin, Y. Chen, Y. Wang, Non-noble metal-based carbon composites in hydrogen evolution reaction: fundamentals to applications, Adv. Mater. 29 (2017), https://doi.org/10.1002/adma.201605838.
[4] P. Yu, F. Wang, T.A. Shifa, X. Zhan, X. Lou, F. Xia, J. He, Earth abundant materials beyond transition metal dichalcogenides: a focus on electrocatalyzing hydrogen evolution reaction, Nano Energy 58 (2019) 244–276, https://doi.org/10.1016/j.nanoen.2019.01.017.
[5] M.I. Jamesh, X. Sun, Recent progress on earth abundant electrocatalysts for oxygen evolution reaction (OER) in alkaline medium to achieve efficient water splitting – a review, J. Power Sources 400 (2018) 31–68, https://doi.org/10.1016/j.jpowsour.2018.07.125.
[6] N.T. Suen, S.F. Hung, Q. Quan, N. Zhang, Y.J. Xu, H.M. Chen, Electrocatalysis for the oxygen evolution reaction: recent development and future perspectives, Chem. Soc. Rev. 46 (2017) 337–365, https://doi.org/10.1039/c6cs00328a.
[7] J. Wang, W. Cui, Q. Liu, Z. Xing, A.M. Asiri, X. Sun, Recent progress in cobalt-based heterogeneous catalysts for electrochemical water splitting, Adv. Mater. 28 (2016) 215–230, https://doi.org/10.1002/adma.201502696.
[8] M. Tahir, L. Pan, F. Idrees, X. Zhang, L. Wang, J.J. Zou, Z.L. Wang, Electrocatalytic oxygen evolution reaction for energy conversion and storage: a comprehensive review, Nano Energy 37 (2017) 136–157, https://doi.org/10.1016/j.nanoen.2017.05.022.
[9] Y. Liang, Y. Li, H. Wang, H. Dai, ChemInform abstract: strongly coupled inorganic/nanocarbon hybrid materials for advanced electrocatalysis, ChemInform 44 (2013), https://doi.org/10.1002/chin.201321224 no-no.
[10] M.H.V. Huynh, T.J. Meyer, Proton-coupled electron transfer, Chem. Rev. 107 (2007) 5004–5064, https://doi.org/10.1021/cr0500030.
[11] C.C.L. McCrory, S. Jung, J.C. Peters, T.F. Jaramillo, Benchmarking heterogeneous electrocatalysts for the oxygen evolution reaction, J. Am. Chem. Soc. 135 (2013) 16977–16987, https://doi.org/10.1021/ja407115p.
[12] M.G. Walter, E.L. Warren, J.R. McKone, S.W. Boettcher, Q. Mi, E.A. Santori, N. S. Lewis, Solar water splitting cells, Chem. Rev. 110 (2010) 6446–6473, https://doi.org/10.1021/cr1002326.
[13] J. Wang, N. Yang, H. Tang, Z. Dong, Q. Jin, M. Yang, D. Kisailus, H. Zhao, Z. Tang, D. Wang, Accurate control of multishelled Co3O4 hollow microspheres as high-performance anode materials in lithium-ion batteries, Angew. Chem. Int. Ed. 52 (2013) 6417–6420, https://doi.org/10.1002/anie.201301622.
[14] X. Yan, L. Tian, K. Li, S. Atkins, H. Zhao, J. Murowchick, L. Liu, X. Chen, FeNi3/NiFeOx nanohybrids as highly efficient bifunctional electrocatalysts for overall

[15] X. Xiong, Y. Ji, M. Xie, C. You, L. Yang, Z. Liu, A.M. Asiri, X. Sun, MnO2-CoP3 nanowires array: an efficient electrocatalyst for alkaline oxygen evolution reaction with enhanced activity, Electrochem. Commun. 86 (2018) 161–165, https://doi.org/10.1016/j.elecom.2017.12.008.
[16] Q. Wang, L. Shang, R. Shi, X. Zhang, G.I.N. Waterhouse, L.Z. Wu, C.H. Tung, T. Zhang, 3D carbon nanoframe scaffold-immobilized Ni3FeN nanoparticle electrocatalysts for rechargeable zinc-air batteries' cathodes, Nano Energy 40 (2017) 382–389, https://doi.org/10.1016/j.nanoen.2017.08.040.
[17] W. Xu, F. Lyu, Y. Bai, A. Gao, J. Feng, Z. Cai, Y. Yin, Porous cobalt oxide nanoplates enriched with oxygen vacancies for oxygen evolution reaction, Nano Energy 43 (2018) 110–116, https://doi.org/10.1016/j.nanoen.2017.11.022.
[18] G. Liu, P. Li, G. Zhao, X. Wang, J. Kong, H. Liu, H. Zhang, K. Chang, X. Meng, T. Kako, J. Ye, Promoting active species generation by plasmon-induced hot-electron excitation for efficient electrocatalytic oxygen evolution, J. Am. Chem. Soc. 138 (2016) 9128–9136, https://doi.org/10.1021/jacs.6b05190.
[19] T. Reier, M. Oezaslan, P. Strasser, Electrocatalytic oxygen evolution reaction (OER) on Ru, Ir, and pt catalysts: a comparative study of nanoparticles and bulk materials, ACS Catal. 2 (2012) 1765–1772, https://doi.org/10.1021/cs3003098.
[20] F. Yuan, X. Cheng, M. Wang, Y. Ni, Controlled synthesis of tubular ferrite MFe2O4 (M = Fe, Co, Ni) microstructures with efficiently electrocatalytic activity for water splitting, Electrochim. Acta 324 (2019) 134883, https://doi.org/10.1016/j.electacta.2019.134883.
[21] M.W. Louie, A.T. Bell, An investigation of thin-film Ni-Fe oxide catalysts for the electrochemical evolution of oxygen, J. Am. Chem. Soc. 135 (2013) 12329–12337, https://doi.org/10.1021/ja405351s.
[22] V. Torabinejad, M. Aliofkhazraei, S. Assareh, M.H. Allahyarzadeh, A. S. Rouhaghdam, Electrodeposition of Ni-Fe alloys, composites, and nano coatings–A review, J. Alloys Compd. 691 (2017) 841–859, https://doi.org/10.1016/j.jallcom.2016.08.329.
[23] R. Solmaz, G. Kardaş, Electrochemical deposition and characterization of NiFe coatings as electrocatalytic materials for alkaline water electrolysis, Electrochim. Acta 54 (2009) 3726–3734, https://doi.org/10.1016/j.electacta.2009.01.064.
[24] Y. Ullal, A.C. Hegde, Electrodeposition and electro-catalytic study of nanocrystalline Ni-Fe alloy, Int. J. Hydrogen Energy 39 (2014) 10485–10492, https://doi.org/10.1016/j.ijhydene.2014.05.016.
[25] X. Shang, J.F. Qin, J.H. Lin, B. Dong, J.Q. Chi, Z.Z. Liu, L. Wang, Y.M. Chai, C. G. Liu, Tuning the morphology and Fe/Ni ratio of a bimetallic Fe-Ni-S film supported on nickel foam for optimized electrolytic water splitting, J. Colloid Interface Sci. 523 (2018) 121–132, https://doi.org/10.1016/j.jcis.2018.03.083.
[26] Q. Luo, M. Peng, X. Sun, Y. Luo, A.M. Asiri, Efficient electrochemical water splitting catalyzed by electrodeposited NiFe nanosheets film, Int. J. Hydrogen Energy 41 (2016) 8785–8792, https://doi.org/10.1016/j.ijhydene.2016.04.007.
[27] Q. Yan, T. Wei, J. Wu, X. Yang, M. Zhu, K. Cheng, K. Ye, K. Zhu, J. Yan, D. Cao, G. Wang, Y. Pan, Self-supported FeNi-P nanosheets with thin amorphous layers for efficient electrocatalytic water splitting, ACS Sustain. Chem. Eng. 6 (2018) 9640–9648, https://doi.org/10.1021/acssuschemeng.7b04743.
[28] D. Friebel, M.W. Louie, M. Bajdich, K.E. Sanwald, Y. Cai, A.M. Wise, M.J. Cheng, D. Sokaras, T.C. Weng, R. Alonso-Mori, R.C. Davis, J.R. Bargar, J.K. Nørskov, A. Nilsson, A.T. Bell, Identification of highly active Fe sites in (Ni,Fe)OOH for electrocatalytic water splitting, J. Am. Chem. Soc. 137 (2015) 1305–1313, https://doi.org/10.1021/ja511559d.
[29] C. Tang, L. Gan, R. Zhang, W. Lu, X. Jiang, A.M. Asiri, X. Sun, J. Wang, L. Chen, Ternary FexCo1-xP nanowire array as a robust hydrogen evolution reaction electrocatalyst with Pt-like activity: experimental and theoretical insight, Nano Lett. 16 (2016) 6617–6621, https://doi.org/10.1021/acs.nanolett.6b03332.
[30] F.A. Lowenheim, Electroplating, McGraw-Hill Companies, New York, 1978.
[31] A.P. Abbott, G. Capper, K.J. McKenzie, K.S. Ryder, Electrodeposition of zinc-tin alloys from deep eutectic solvents based on choline chloride, J. Electroanal. Chem. 599 (2007) 288–294, https://doi.org/10.1016/j.jelechem.2006.04.024.
[32] L. Vieira, R. Schennach, B. Gollas, The effect of the electrode material on the electrodeposition of zinc from deep eutectic solvents, Electrochim. Acta 197 (2016) 344–352, https://doi.org/10.1016/j.electacta.2015.11.030.
[33] X. Cao, L. Xu, Y. Shi, Y. Wang, X. Xue, Electrochemical behavior and electrodeposition of cobalt from choline chloride-urea deep eutectic solvent, Electrochim. Acta 295 (2019) 550–557, https://doi.org/10.1016/j.electacta.2018.10.163.
[34] J. Winiarski, B. Cieślikowska, W. Tylus, P. Kunicki, B. Szczygieł, Corrosion of nanocrystalline nickel coatings electrodeposited from choline chloride: ethylene glycol deep eutectic solvent exposed in 0.05 M NaCl solution, Appl. Surf. Sci. 470 (2019) 331–339, https://doi.org/10.1016/j.apsusc.2018.11.155.
[35] S. Rao, X. Zou, S. Wang, Y. Lu, T. Shi, H.Y. Hsu, Q. Xu, X. Lu, Electrodeposition of Ni-Cu alloy films from nickel matte in deep eutectic solvent, Mater. Chem. Phys. 232 (2019) 6–15, https://doi.org/10.1016/j.matchemphys.2019.04.052.
[36] S. Wang, X. Zou, Y. Lu, S. Rao, X. Xie, Z. Pang, X. Lu, Q. Xu, Z. Zhou, Electrodeposition of nano-nickel in deep eutectic solvents for hydrogen evolution reaction in alkaline solution, Int. J. Hydrogen Energy 43 (2018) 15673–15686, https://doi.org/10.1016/j.ijhydene.2018.06.188.
[37] G. Saravanan, S. Mohan, Structure, composition and corrosion resistance studies of Co-Cr alloy electrodeposited from deep eutectic solvent (DES), J. Alloys Compd. 522 (2012) 162–166, https://doi.org/10.1016/j.jallcom.2012.01.140.
[38] A.P. Abbott, M. Azam, K.S. Ryder, S. Saleem, Study of silver electrodeposition in deep eutectic solvents using atomic force microscopy, Trans. Inst. Met. Finish. 96 (2018) 297–303, https://doi.org/10.1080/00202967.2018.1520483.

[39] Q. Zhang, K. De Oliveira Vigier, S. Royer, F. Jérôme, Deep eutectic solvents: syntheses, properties and applications, Chem. Soc. Rev. 41 (2012) 7108–7146, https://doi.org/10.1039/c2cs35178a.

[40] A. Paiva, R. Craveiro, I. Aroso, M. Martins, R.L. Reis, A.R.C. Duarte, Natural deep eutectic solvents - solvents for the 21st century, ACS Sustain. Chem. Eng. 2 (2014) 1063–1071, https://doi.org/10.1021/sc500096j.

[41] A.P. Abbott, D. Boothby, G. Capper, D.L. Davies, R.K. Rasheed, Deep Eutectic Solvents formed between choline chloride and carboxylic acids: versatile alternatives to ionic liquids, J. Am. Chem. Soc. 126 (2004) 9142–9147, https://doi.org/10.1021/ja048266j.

[42] A.P. Abbott, G. Capper, D.L. Davies, R.K. Rasheed, V. Tambyrajah, Novel solvent properties of choline chloride/urea mixtures, Chem. Commun. (2003) 70–71, https://doi.org/10.1039/b210714g.

[43] T. Yanai, T. Akiyoshi, T. Yamaguchi, K. Takashima, T. Morimura, M. Nakano, H. Fukunaga, Effect of primary amines on magnetic properties of Fe-Ni films electroplated in a DES-based plating bath, AIP Adv. 8 (2018), https://doi.org/10.1063/1.5007189.

[44] R. Boggio, A. Carugati, S. Trasatti, Electrochemical surface properties of Co3O4 electrodes, J. Appl. Electrochem. 17 (1987) 828–840.

[45] S. Trasatti, O.A. Petrii, Real surface area measurements in electrochemistry, Pure Appl. Chem. 63 (1991) 711–734.

[46] J.S. Sagu, D. Mehta, K.G.U. Wijayantha, Electrocatalytic activity of CoFe2O4 thin films prepared by AACVD towards the oxygen evolution reaction in alkaline media, Electrochem. Commun. 87 (2018) 1–4, https://doi.org/10.1016/j.elecom.2017.12.017.

[47] S. Anantharaj, S.R. Ede, K. Karthick, S. Sam Sankar, K. Sangeetha, P.E. Karthik, S. Kundu, Precision and correctness in the evaluation of electrocatalytic water splitting: revisiting activity parameters with a critical assessment, Energy Environ. Sci. 11 (2018) 744–771, https://doi.org/10.1039/c7ee03457a.

[48] M. Khalid, A.M.B. Honorato, G. Tremiliosi Filho, H. Varela, Trifunctional catalytic activities of trimetallic FeCoNi alloy nanoparticles embedded in a carbon shell for efficient overall water splitting, J. Mater. Chem. A. 8 (2020) 9021–9031, https://doi.org/10.1039/c9ta13637a.

[49] R.A. Nickell, W.H. Zhu, R.U. Payne, D.R. Cahela, B.J. Tatarchuk, Hg/HgO electrode and hydrogen evolution potentials in aqueous sodium hydroxide, J. Power Sources 161 (2006) 1217–1224, https://doi.org/10.1016/j.jpowsour.2006.05.028.

[50] J. Balej, Determination of the oxygen and hydrogen overvoltage in concentrated alkali hydroxide solutions, Int. J. Hydrogen Energy 10 (1985) 365–374, https://doi.org/10.1016/0360-3199(85)90062-X.

[51] Z. Ghaferi, S. Sharafi, M.E. Bahrololoom, Effect of current density and bath composition on crystalline structure and magnetic properties of electrodeposited FeCoW alloy, Appl. Surf. Sci. 355 (2015) 766–773, https://doi.org/10.1016/j.apsusc.2015.07.083.

[52] M. Tavoosi, A. Barahimi, Corrosion behavior of amorphous–nanocrystalline Fe–Ni–Cr electrodeposited coatings, Surface. Interfac. 8 (2017) 103–111, https://doi.org/10.1016/j.surfin.2017.05.004.

[53] W. Lu, M. Jia, M. Ling, Y. Xu, J. Shi, X. Fang, Y. Song, X. Li, Phase evolution and magnetic properties of FeCo films electrodeposited at different temperatures, J. Alloys Compd. 637 (2015) 552–556, https://doi.org/10.1016/j.jallcom.2015.03.036.

[54] W. Sides, N. Kassouf, Q. Huang, Electrodeposition of ferromagnetic FeCo and FeCoMn alloy from choline chloride based deep eutectic solvent, J. Electrochem. Soc. 166 (2019) D77–D85, https://doi.org/10.1149/2.0181904jes.

[55] P. Lammel, L.D. Rafailovic, M. Kolb, K. Pohl, A.H. Whitehead, G. Grundmeier, B. Gollas, Analysis of rain erosion resistance of electroplated nickel-tungsten alloy coatings, Surf. Coating. Technol. 206 (2012) 2545–2551, https://doi.org/10.1016/j.surfcoat.2011.11.009.

[56] N. Eliaz, T.M. Sridhar, E. Gileadi, Synthesis and characterization of nickel tungsten alloys by electrodeposition, Electrochim. Acta 50 (2005) 2893–2904, https://doi.org/10.1016/j.electacta.2004.11.038.

[57] L. Vieira, R. Schennach, B. Gollas, In situ PM-IRRAS of a glassy carbon electrode/deep eutectic solvent interface, Phys. Chem. Chem. Phys. 17 (2015) 12870–12880, https://doi.org/10.1039/c5cp00070j.

[58] S.S. Maklakov, S.A. Maklakov, I.A. Ryzhikov, V.A. Amelichev, K.V. Pokholok, A. N. Lagarkov, Mössbauer study of disordering in thin sputtered FeCo-SiO2 and FeCo films, J. Alloys Compd. 536 (2012) 33–37, https://doi.org/10.1016/j.jallcom.2012.05.022.

[59] P. Crespo, N. Menéndez, J.D. Tornero, M.J. Barro, J.M. Barandiarán, A. García Escorial, A. Hernando, Mössbauer spectroscopy evidence of a spinodal mechanism for the thermal decomposition of F.C.C. FeCu, Acta Mater. 46 (1998) 4161–4166, https://doi.org/10.1016/S1359-6454(98)00111-6.

[60] C.E. Johnson, M.S. Ridout, T.E. Cranshaw, The Mössbauer effect in iron alloys, Proc. Phys. Soc. 81 (1963) 1079–1090, https://doi.org/10.1088/0370-1328/81/6/313.

[61] A. Kozlovskiy, A. Zhanbotin, M. Zdorovets, I. Manakova, A. Ozernoy, K. Kadyrzhanov, V. Rusakov, Study of Ni/Fe nanotube properties, Nucl. Instrum. Methods Phys. Res. Sect. B Beam Interact. Mater. Atoms 365 (2015) 663–667, https://doi.org/10.1016/j.nimb.2015.09.090.

[62] V.A.P. Rodríguez, C. Rojas-Ayala, J.M. Medina, P.P. Cabrera, J. Quispe-Marcatoma, C.V. Landauro, J.R. Tapia, E.M. Baggio-Saitovitch, E.C. Passamani, Fe 50 Ni 50 synthesized by high energy ball milling: a systematic study using X-ray diffraction, EXAFS and Mössbauer methods, Mater. Char. 149 (2019) 249–254, https://doi.org/10.1016/j.matchar.2019.01.036.

[63] A. Guittoum, A. Layadi, A. Bourzami, H. Tafat, N. Souami, S. Boutarfaia, D. Lacour, X-ray diffraction, microstructure, Mössbauer and magnetization studies of nanostructured Fe50Ni50 alloy prepared by mechanical alloying, J. Magn. Magn Mater. 320 (2008) 1385–1392, https://doi.org/10.1016/j.jmmm.2007.11.021.

[64] E. Lima, V. Drago, A new process to produce ordered Fe50Ni50 tetrataenite, Phys. Status Solidi Appl. Res. 187 (2001) 119–124, https://doi.org/10.1002/1521-396X(200109)187:1<119::AID-PSSA119>3.0.CO;2-L.

[65] Y.A. Abdu, H. Annersten, T. Ericsson, P. Nordblad, Field-induced local magnetic moments in γ (FCC) Fe-Ni anti-Invar alloys, J. Magn. Magn Mater. 280 (2004) 243–250, https://doi.org/10.1016/j.jmmm.2004.03.019.

[66] F.G.S. Oliveira, F. Bohn, A.N. Correia, I.F. Vasconcelos, P. de Lima-Neto, Fe–Co coatings electrodeposited from eutectic mixture of choline chloride-urea: physical characterizations and evaluation as electrocatalysts for the hydrogen evolution reaction, J. Alloys Compd. 851 (2021), https://doi.org/10.1016/j.jallcom.2020.156330.

[67] K.V. Frolov, D.L. Zagorskii, I.S. Lyubutin, M.A. Chuev, I.V. Perunov, S.A. Bedin, A. A. Lomov, V.V. Artemov, S.N. Sulyanov, Magnetic and structural properties of Fe–Co nanowires fabricated by matrix synthesis in the pores of track membranes, JETP Lett. (Engl. Transl.) 105 (2017) 319–326, https://doi.org/10.1134/S0021364017050083.

[68] D. Cao, Z. Wang, E. Feng, J. Wei, J. Wang, Q. Liu, Magnetic properties and microstructure investigation of electrodeposited FeNi/ITO films with different thickness, J. Alloys Compd. 581 (2013) 66–70, https://doi.org/10.1016/j.jallcom.2013.07.050.

[69] N. Mansouri, N. Benbrahim-Cherief, E. Chainet, F. Charlot, T. Encinas, S. Boudinar, B. Benfedda, L. Hamadou, A. Kadri, Electrodeposition of equiatomic FeNi and FeCo nanowires: structural and magnetic properties, J. Magn. Magn Mater. 493 (2020) 165746, https://doi.org/10.1016/j.jmmm.2019.165746.

[70] J. Zhu, L. Hu, P. Zhao, L.Y.S. Lee, K.Y. Wong, Recent advances in electrocatalytic hydrogen evolution using nanoparticles, Chem. Rev. 120 (2020) 851–918, https://doi.org/10.1021/acs.chemrev.9b00248.

[71] Z. Ma, R. Li, M. Wang, H. Meng, F. Zhang, X.Q. Bao, B. Tang, X. Wang, Self-supported porous Ni-Fe-P composite as an efficient electrocatalyst for hydrogen evolution reaction in both acidic and alkaline medium, Acta 219 (2016) 194–203, https://doi.org/10.1016/j.electacta.2016.10.004.

[72] Y. Yang, K. Zhang, H. Lin, X. Li, H.C. Chan, L. Yang, Q. Gao, MoS2-Ni3S2 heteronanorods as efficient and stable bifunctional electrocatalysts for overall water splitting, ACS Catal. 7 (2017) 2357–2366, https://doi.org/10.1021/acscatal.6b03192.

[73] L. Trotochaud, S.L. Young, J.K. Ranney, S.W. Boettcher, Nickel-Iron oxyhydroxide oxygen-evolution electrocatalysts: the role of intentional and incidental iron incorporation, J. Am. Chem. Soc. 136 (2014) 6744–6753, https://doi.org/10.1021/ja502379c.

[74] T.G. Vo, S.D.S. Hidalgo, C.Y. Chiang, Controllable electrodeposition of binary metal films from deep eutectic solvent as an efficient and durable catalyst for the oxygen evolution reaction, Dalton Trans. 48 (2019) 14748–14757, https://doi.org/10.1039/c9dt03028j.

[75] Y. Qiu, L. Xin, W. Li, Electrocatalytic oxygen evolution over supported small amorphous ni-fe nanoparticles in alkaline electrolyte, Langmuir 30 (2014) 7893–7901, https://doi.org/10.1021/la501246e.

[76] C. Chen, Z. Yang, W. Liang, H. Yan, Y. Tuo, Y. Li, Y. Zhou, J. Zhang, Ultra-small Co/CoOx nanoparticles dispersed on N-doped carbon nanosheets for highly efficient electrocatalytic oxygen evolution reaction, J. Energy Chem. 55 (2021) 345–354, https://doi.org/10.1016/j.jechem.2020.07.017.

[77] T.F. O'Brien, T.V. Bommaraju, F. Hine, Overview of the chlor-alkali industry, in: Handbook of Chlor-Alkali Technology, vol. I, Springer science, Boston, 2005.

[78] C. Dong, X. Yuan, X. Wang, X. Liu, W. Dong, R. Wang, Y. Duan, F. Huang, Rational design of cobalt-chromium layered double hydroxide as a highly efficient electrocatalyst for water oxidation, J. Mater. Chem. A. 4 (2016) 11292–11298, https://doi.org/10.1039/c6ta04052g.

[79] T. Liu, X. Sun, A.M. Asiri, Y. He, One-step electrodeposition of Ni-Co-S nanosheets film as a bifunctional electrocatalyst for efficient water splitting, Int. J. Hydrogen Energy 41 (2016) 7264–7269, https://doi.org/10.1016/j.ijhydene.2016.03.111.

[80] T. Liu, A.M. Asiri, X. Sun, Electrodeposited Co-doped NiSe2 nanoparticles film: a good electrocatalyst for efficient water splitting, Nanoscale 8 (2016) 3911–3915, https://doi.org/10.1039/c5nr07170d.